# Asymptotically single-mode small-core terahertz Bragg fibre with low loss and low dispersion

## B Hong, M Swithenbank, N Somjit, J Cunningham, and I Robertson

School of Electronic and Electrical Engineering, University of Leeds, Leeds LS2 9JT, UK

E-mail: elbho@leeds.ac.uk; i.d.robertson@leeds.ac.uk

**Abstract**

This paper presents a novel design concept, which is verified by analytical and simulation results, of a single-mode small-core terahertz Bragg fibre exhibiting the properties of low loss and low dispersion. Conventionally, a single-$TE_{01}$-mode Bragg fibre requires a large core and many cladding layer periods to achieve a significant propagation loss discrimination between the desired mode and other unwanted competing modes. The use of a second-order bandgap in this paper completely eliminates this requirement, and enhances propagation loss discrimination using just a small core with a diameter at least 50% smaller than the conventional design and only four cladding layer periods. Furthermore, a generalized half-wavelength condition is proposed, promoting the manipulation of photonic bandgap for Bragg fibre. The $TE_{01}$ mode has a null point in the electric field close to the boundary interface between the core and the cladding, and this phenomenon has been exploited to minimize the impact of support bridges, which mechanically maintain the air gaps, on the propagation loss of the fibre. Finally, we propose a novel design of a tightly confined single-$TE_{01}$-mode small-air-core Bragg fibre with propagation loss and group velocity dispersion less than 1.2 dB/m and -0.6 ps/THz/cm, respectively, between frequencies of 0.85 THz and 1.15 THz.

Keywords: Bragg fibre, electromagnetic propagation, half-wavelength condition, low-loss, modal-filtering effect, single-mode.

## 1. Introduction

THz waveguides show great potential as replacements for the bulky optical measurement systems typically used in terahertz time-domain spectroscopy (THz-TDS) systems. They offer potential benefits in allowing tight electromagnetic (EM) mode confinement to structures smaller than the Rayleigh limit, resulting in spatial resolution enhancements over various free-space THz systems [1, 2].

The realization of tightly confined single-mode THz waveguides with both low losses and low dispersion has proved challenging, since metals and most dielectric materials have high material losses in the THz frequency range [3-5]. Microstructured fibres, including photonic crystal fibres and index guided fibres, have been intensively studied in the optical frequency range [6] and recently became an active topic of research into THz waveguide [7-21]. A comprehensive summary of the propagation loss of state-of-the-art on THz microstuctured fibres is presented in figure 1. It is notable that low-loss single-mode THz microstructured fibre around 1 THz is still not available.

In addition, other efforts have been made towards the development of low-loss THz waveguides and fibres. Hollow metallic waveguides [22, 23] suffer high ohmic loss and large group velocity dispersion (GVD) at terahertz frequencies. Optical fibre is limited by dielectric absorption at THz frequencies since both glasses and polymers have high THz absorption. Recent work [24] on polymer tubes shows that 20 dB/m propagation loss can be achieved over a wide THz band. However, as the EM field can leak into the lossy cladding material, the overall signal loss is still high, and it suffers from mode competition due to its overmoded structure. Planar and coaxial transmission lines [25-27], including spoof waveguide, usually suffer from various effects e.g. ohmic loss, dielectric absorption, and radiation loss, which together combine to make them very lossy at terahertz frequencies. Bare metal wire [28, 29] and sub-wavelength polymer fibre [30] show a relatively low loss, and low dispersion, but
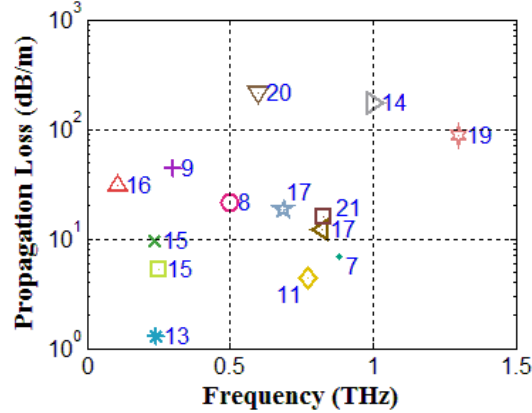
Figure 1. Review of the propagation loss of experimental works on THz microstructured fibre. The number next to the symbol is the reference number of that work. Some papers present different works in same paper. The minimum loss point has been chosen to present each work. References [13] and [17] are air core Bragg fibres.

they suffer from radiation loss and environmental disturbance, such as moisture in the air and cladding roughness. Parallel-plate waveguide [31, 32] exhibits extremely low loss with negligible dispersion and single mode property over a wide band, but it suffers from radiation loss since the field is not tightly confined in the open lateral direction. Coating the inside of a cylindrical metallic waveguide with a thin dielectric layer reduces its propagation loss [33, 34]. However, the waveguides usually operate in an overmoded configuration, and therefore suffer from mode competition due to poor mode selectivity. Both dielectric-filled and hollow substrate integrated waveguide (HSIW) provide a promising platform for millimetre-wave integrated circuits due to their ease of integration and printability [35, 36]. However, at THz frequencies, the loss of dielectric-filled substrate integrated waveguide (SIW) is mainly limited by high material absorption loss [35], while the loss of HSIW converges to the high ohmic loss [36]. In addition, the metal vias are very difficult to make, especially in the THz range. Photonic crystal slab waveguides [37-39] show very low loss, but their effective bandwidths are usually only several GHz which are relatively narrow.

Reducing the propagation loss is of primary interest for a THz waveguide, because it is currently not easy to generate continuous-wave (CW) signal power over 1 mW near 1 THz in compact THz systems. Since the lowest THz absorption loss occurs for dry air, it is essential for a THz waveguide to maximize the guided signal power in the air volume. An air-core Bragg fibre [40] is capable of tightly confining EM waves in a lossless dry air core, consequently reducing the propagation loss. Large-air-core Bragg fibre has been proven to support the transmission of optical signal with losses less than 1 dB/m [41, 42]. Recently, some efforts [13, 17] towards the development of low-loss air-core THz Bragg fibre have been made but their losses are still relatively high near 1 THz, as shown in figure 1.

This paper proposes a novel design of single-$TE_{01}$-mode small-air-core Bragg fibre working from 0.85 THz to 1.15 THz. It is composed of concentric dielectric layers in air, separated by support bridges. The support bridges act as defects in the photonic crystal structure which can cause mode coupling between the core mode and the surface states, resulting in an the increasing of the propagation loss [43]. However, the proposed single-$TE_{01}$-mode Bragg fibre, which has a null point in the electric field close to the interface between the core and the cladding, can greatly suppress the negative impact of the support bridges on the propagation loss, exhibiting strong superiority over single-$HE_{11}$-mode Bragg fibre. In addition, unlike conventional single-$TE_{01}$-mode Bragg fibre which requires a large core, whose diameter is about 7.5 times of the operational wavelength, and 8 cladding layer periods [44], the single-$TE_{01}$-mode Bragg fibre in this paper utilise a much smaller core, whose diameter is about 3 times the operational wavelength, and just 4 cladding layer periods. Thus, both the overall size of the Bragg fibre and the need for support bridges for mechanically maintaining the air gaps are greatly reduced. Moreover, the loss discrimination between the desired mode and other unwanted competing modes in our design is about 3 times larger than that of the conventional design [42], resulting in better mode selectivity. Furthermore, we also proposed a generalized half-wavelength condition describing the relationship between the material properties, the geometry, and the photonic bandgap, which provides an efficient technique to manipulate the shape of the photonic bandgap for Bragg fibre. Our theoretical calculations indicate that the proposed Bragg fibre can achieve propagation loss less than 1.2 dB/m between frequencies from 0.85 THz to 1.15 THz with only 4 cladding layer periods, which makes it a strong candidate for low loss guidance of THz wave.
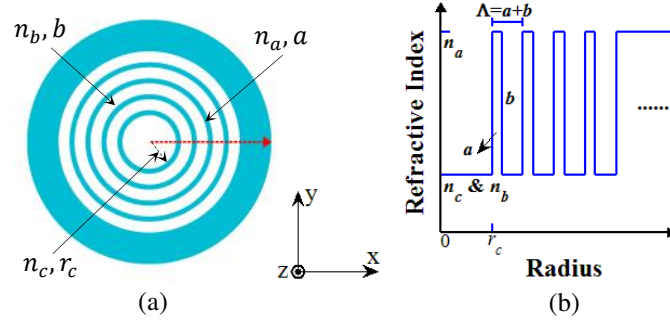
Figure 2. Schematic of an ideal Bragg fibre. (a) The transverse section of the Bragg fibre which is uniform along the z-axis. (b) The radial refractive index profile of the Bragg fibre along the red dashed arrow in (a) starting from the centre and going into the edge.

## 2. Manipulation of photonic bandgap for Bragg fibre

Figure 2 shows the geometry and the refractive index profile of the proposed Bragg fibre. It comprises an air core ($n_c = 1$) cladded surrounded by periodic concentric dielectric layers of alternatively high ($n_a$) and low ($n_b$) refractive index materials, the thickness of which are $a$ and $b$ respectively, while $r_c$ is the core radius and $\Lambda = a + b$ is the period of the radial photonic crystal. The outermost layer is a thick protective layer that will absorb any residual EM waves and isolate the fibre from external perturbations. In this paper, Bragg fibres that use air as the core and low refractive index material are investigated, so $n_b = n_c = 1$. There are at least four key advantages for this type of Bragg fibre compared to others with $n_b > 1$ : (1) Owing to the high porosity, the vast majority of the THz wave is distributed in lossless dry air; (2) The width of the bandgap is maximized by cladding materials with a high refractive index contrast [45]; (3) Our Bragg fibres with $n_b = 1$ show filtering of the unwanted TM modes owing to the Brewster phenomenon [46]; (4) The fabrication process is simplified since the concept is based on only one material, e.g. fabrication by extrusion or drawing. As a result of this, some support bridges or struts are required in order to maintain the air gaps between the dielectric claddings, however. As it is impractical to analyse analytically a practical Bragg fibre with support bridges, we begin first with an analysis of the ideal Bragg fibre without support bridges, before the impact of the support bridges on the Bragg fibre is discussed (in section 3.5).

In order to understand the EM-field confinement mechanism, we first discuss how the band diagram is obtained. According to the Bloch's theorem in cylindrical coordinates [47], the constraint which stops the EM field from propagating through into the cladding crystal can be expressed as

$$|\mathbf{Re}(X_s)| < 1 \tag{1}$$

where

$$X_s = \left[ \cos(k_b b) - \frac{i}{2} \left( \frac{\zeta_b k_b}{\zeta_a k_a} + \frac{\zeta_a k_a}{\zeta_b k_b} \right) \sin(k_b b) \right] \exp(-i k_a a) \tag{2}$$

and $k_i = \sqrt{(n_i k_0)^2 - \beta^2}$ ($i = a, b, c$) is the lateral propagation constant; $k_0 = \omega/c$ is the vacuum wavenumber; $\omega$ is the vacuum angular frequency; $c$ is the speed of light in vacuum; $\beta$ is the longitudinal constant, $\beta/k_0$ is the effective refractive index of the mode ($n_{eff}$), and $\zeta_i$ is 1 or $1/n_i^2$ ($i = a, b$) corresponding to TE or TM modes respectively.

The bandgap equation (1) can be solved analytically once the geometric ($a, b, r_c$) and materials ($n_a, n_b, n_c$) parameters are

Table 1. Quarter-wavelength conditions

| Quarter-wavelength condition | Angle of Incidence |
|---|---|
| $a n_a = b n_b = \lambda_t/4$ | $\theta = 0°$ |
| $a\sqrt{n_a^2 - 1} = b\sqrt{n_b^2 - 1} = \lambda_t/4$ | $\theta = 90°$ |
| $a\sqrt{n_a^2 - n_t^2} = b\sqrt{n_b^2 - n_t^2} = \lambda_t/4$ | $\theta = \mathrm{asin}(n_t)$ |

both known. The quarter-wavelength condition (QWC) has been widely used as a guiding principle to choose the layer thickness [44, 45, 48, 49], as shown in table 1. Here, $\lambda_t$ is a wavelength of interest which is equal or close to the central wavelength of the photonic bandgap, $n_t = \beta/k_0$ indicates the effective refractive index of interest, and $\theta$ is the angle of incidence between the normal line of the surface and the direction of the wavenumber in the plane of incidence. There are at least two disadvantages with the aforementioned QWC treatment: firstly, the QWC only applies for the first order bandgap and thus cannot be used to manipulate higher order bandgaps; secondly, the QWC only maximizes the first order bandgap by making the thicknesses of the cladding layers equal to one quarter of the wavelength of interest; thus, it cannot be used to tune the bandwidth. In practical terms, it is highly desirable that the bandwidth and the shape of any order bandgap can be manipulated for the sake of maximizing the confinement of the desired guiding mode as well as filtering out its competing modes. Therefore, a more flexible and multifunctional design principle than the use of the QWC is required.

## 2.1. The generalized half-wavelength condition

In order to manipulate the shape of the bandgap in the Bragg fibre, we here introduce a generalized half-wavelength condition (GHWC), which can be expressed as follows:

$$n_{at}a + n_{bt}b = \zeta \frac{\lambda_t}{2} \tag{3}$$

where

$$n_{at} = \sqrt{n_a^2 - n_t^2} \tag{4}$$

$$n_{bt} = \sqrt{n_b^2 - n_t^2} \tag{5}$$

Here, $\zeta$ is an integer indicating the order number of the bandgap. By introducing a porosity factor $\tau$, equation (3) can be split into the following two equations:

$$n_{at}a = \tau \times \zeta \frac{\lambda_t}{2} \tag{6}$$

$$n_{bt}b = (1 - \tau) \times \zeta \frac{\lambda_t}{2} \tag{7}$$

Therefore, one can obtain the thicknesses of the cladding when the wavelength and effective refractive index of interest are determined. It is noted that if we select $\tau = 0.5$ and $\zeta = 1$, the GHWC reverts to the QWC. Thus, the proposed GHWC also covers all solutions provided by the QWC.

As discussed, we are interested in $n_b = n_c = 1$. Generally, a large $n_a$ increases the refractive index contrast of the cladding layers which enables a larger maximum bandgap resulting in greater EM-field confinement in the core [40]. However, the imaginary part of $n_a$ which accounts for material absorption also significantly influences the performance. At THz frequencies, the choices available for low loss dielectric materials are limited. Silica, which functions well for optical and far infrared applications, has a high loss at THz frequencies [3]. High resistivity silicon shows low loss [50], but does not permit fabrication of fibres. TOPAS is known as a low loss and dispersionless polymer material over the frequency range from 0.2-1.5 THz [3, 7, 8], so we chose this as a representative practical dielectric in our design. We note that the measurement results of the refractive index of TOPAS in [7] are in good agreement with that in [8], but there are still some minor differences between them. In this paper, we choose to use the more recent measurement results in [7]. Namely, we set the real part of the refractive index of TOPAS to 1.5235, and take its absorption coefficient as $\mu$ (dB/cm) $= -0.13 + 0.63(f/1 \times 10^{12}) + (f/1 \times 10^{12})^2$ from 0.2 to 1.5 THz. Here, $f$ is the frequency in Hz. However, it is also of interest to investigate the impact of the uncertainty of the refractive index of TOPAS on the performance of our design, so we address this issue in section 3.3.

Substituting equations (6) and (7) into equation (1) and solving it, the dependence of the bandwidth on $n_t$ and $\tau$ for different $\zeta$ and different polarisations can be obtained (Figure 3). The bandwidth is defined as the midrange ratio of the bandgap, $\Delta = (f_h - f_l)/[1/2(f_h + f_l)]$, when $n_{eff} = n_t$. Here, $f_h$ and $f_l$ are the upper and lower edge of the bandgap, respectively. From figure 3, the bandgap for TE modes always expands when $n_t$ increases, while the bandgap for TM modes first shrinks but then expands after a critical point, where the TM bandgap closes up completely. This critical point, $n_B$, is related to the Brewster angle $\theta_B = \mathrm{asin}(n_B) = \mathrm{asin}(n_a n_b/\sqrt{n_a^2 + n_b^2})$, according to the Brewster phenomenon for TM/EH modes in Bragg fibre. In our case, since $n_a = 1.5235$ and $n_b = 1$, we calculate that $n_B = 0.836$. The Brewster phenomenon reduces the width of the
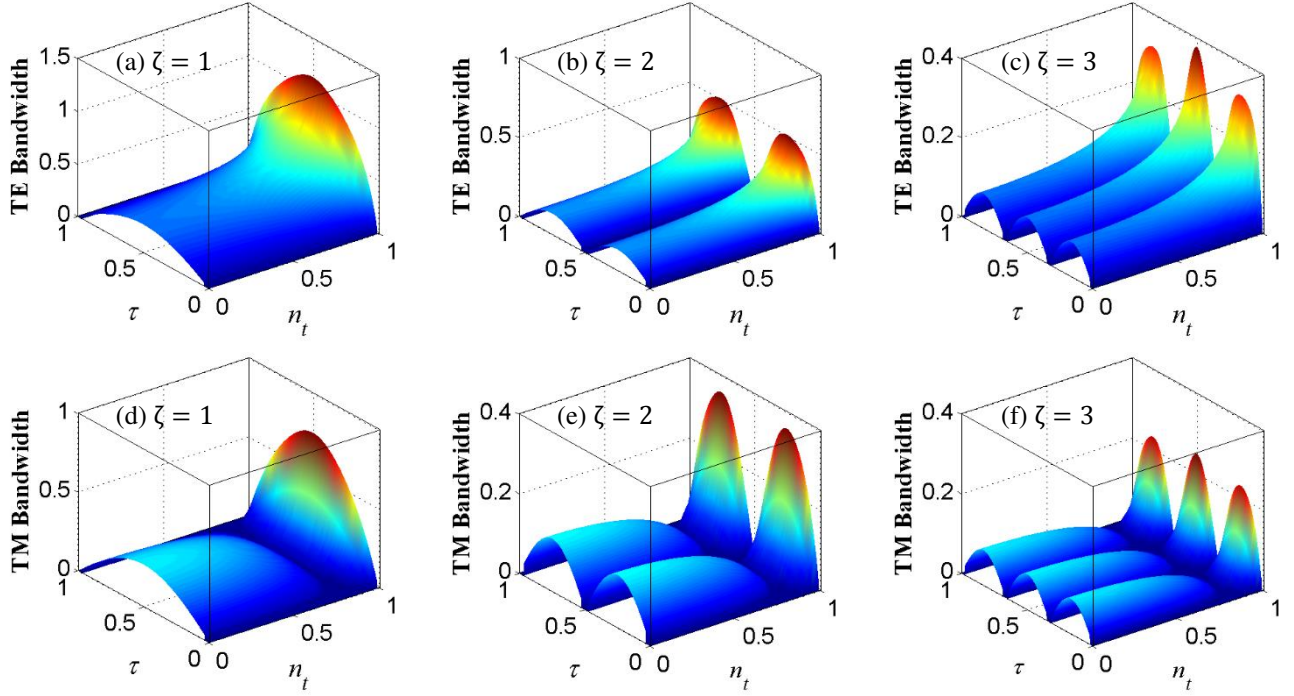
Figure 3. The dependence of midrange ratio bandwidth $\Delta$ on porosity factor $\tau$ and effective refractive index of interest $n_t$ for different polarisations and different bandgap orders $\zeta$. (a)-(c) correspond to TE/HE polarisations. (d)-(e) correspond to TM/EH polarisations. $n_a = 1.5235$, $n_b = 1$, and the thicknesses $a$ and $b$ are calculated by equations (9) and (10). The colour map represents the normalized value of bandwidth, decreasing from red to blue.

bandgap for TM/EH modes, but does not affect the TE/HE bandwidth. The bandwidth for TM/EH modes is always narrower than that of TE/HE modes for the same $n_t$, especially near the Brewster angle. This reduces the EM-field confinement of the TM modes and helps to filter them out, which has also been discussed in our previous work [12].

Owing to the Brewster phenomenon, the bandgaps of the TM/EH modes are always narrower than those of the TE/HE modes, resulting in a leaky propagation of TM/EH modes in a Bragg fibre. Thus, we are more interested in the bandgap for the TE/HE modes. Comparing figures 3 (a), (b) and (c), we find that for the same $n_t$ the bandwidth of the lower order bandgap is generally wider than that of the higher order bandgap. This is validated by calculating and plotting the bandwidth for different order bandgaps in the same diagram by using equation (1) in figure 4. Since the modes of interest in our design lie close to $n_{eff} = 0.95$, we use $n_t = 0.95$ in figure 4. The maximum bandwidth for the 1$^{st}$-order bandgap occurs when $\tau = 0.5$, which
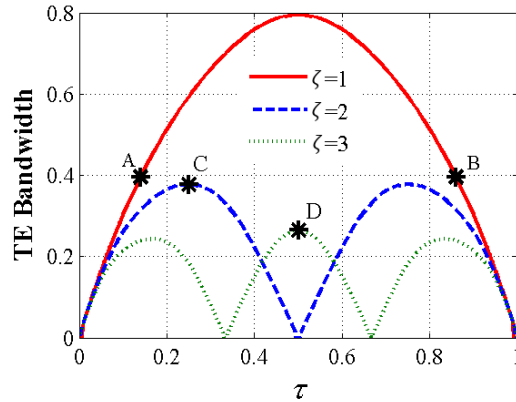


Figure 4. The dependence of midrange ratio bandwidth $\Delta$ on the porosity factor $\tau$ for different bandgap orders number for TE polarisation. $n_a = 1.5235$, $n_b = 1$ and $n_t = 0.95$. The coordinates of A and B are (0.14, 0.3961) and (0.86, 0.3961) respectively.
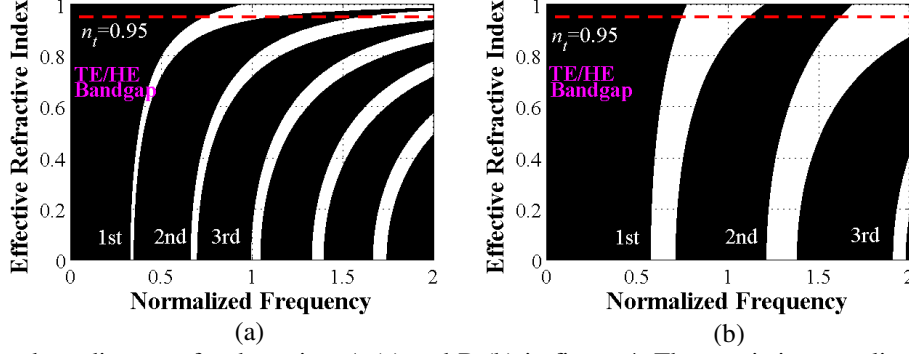
Figure 5. TE/HE bandgap diagrams for the points A (a) and B (b) in figure 4. The x-axis is normalized to the frequency of interest $f_t(= c/\lambda_t)$. The red dashed line indicates the target effective refractive index of interest $n_t = 0.95$. The upper and lower edge of the 1$^{st}$ order bandgaps for both points A and B are $f_h = 1.1143$ and $f_l = 0.7459$ when $n_t = 0.95$. Thus, the midrange ratio bandwidth is $\Delta = 0.3961$. The black region represents the bandpass region for TE/HE modes.

satisfies the QWC. In addition, for any given centre frequency of interest, the maximum bandwidth of the 1$^{st}$-order bandgap is almost twice that of the 2$^{nd}$-order bandgap, three times that of the 3$^{rd}$-order bandgap, *etc*. For a given bandwidth, a higher order bandgap offers a wider range of possible values of $\tau$. If we exclude $\tau = 0$ and $\tau = 1$, which indicate that the thickness of one material in the photonic crystal is zero, it can be seen that $\zeta$th order bandgap has $\zeta - 1$ closing point(s) when $\tau$ sweeps from 0 to 1. Moreover, for both TE and TM bandgaps, the bandwidth of the $\zeta$th ($\zeta = 1,2,3$) order bandgap has $\zeta$ peaks for any certain value of $n_t$.

## 2.2. Representative cases

The points A and B in figure 4 have the same bandwidth, but their bandgap structure is very different, as shown in figure 5. In figure 5, the black region represents the bandpass region for TE/HE modes in which the modes are allowed to propagate through the cladding periodic structure and are not confined in the fibre. The remaining white region shows the bandstop region, defining the bandgap for TE/HE modes. Figures 5 (a) and (b) represent the points A and B in figure 4, respectively. The upper and lower edge of the 1$^{st}$-order bandgaps at $n_{eff} = n_t = 0.95$ for both of them are $f_h = 1.1143$ and $f_l = 0.7459$. Thus the midrange ratio bandwidth is $\Delta = 0.3961$ which is the same as the value obtained in figure 4. Although the centre frequency of the 1$^{st}$-order bandgaps at $n_t = 0.95$ shifts slightly from 1 to 0.93, it can then be tuned back by slightly changing the wavelength of interest $\lambda_t$ in equations (6) and (7) so that the target frequency can be achieved. When the effective refractive index $n_{eff}$ is swept from 0 to 1 in figure 5, the 1$^{st}$-order bandgap shape of figure 5 (a) (point A) is narrower than that of figure 5 (b) (point B) when $n_{eff} < n_t$, but when $n_{eff} > n_t$, conversely, the bandgap width of the 1$^{st}$-order bandgap in figure 5 (a) is wider than that in figure 5 (b). Furthermore, the 1$^{st}$-order bandgap of figure 5 (a) spans several octaves in frequency, which is much wider than that of figure 5 (b). The different behaviours between the points A and B are important differences in the Bragg fibre in terms of manipulating the shape of the bandgap.

In practical terms, we also need to consider the thickness contrast between the cladding layers, as well as their absolute values. According to the GHWC, the thickness contrast between the claddings can be derived from the equations (6) and (7):

$$\frac{b}{a} = \frac{n_{at}(1 - \tau)}{n_{bt}\tau} \tag{8}$$

In accordance with figures 4 and 5, we select $n_t = 0.95$, $n_a = 1.5235$ and $n_b = 1$, thus $n_{at} = 1.1910$ and $n_{bt} = 0.3122$, and the thickness contrast becomes $b/a = 3.8143 \times (1/\tau - 1)$ which has an inverse relationship with $\tau$. As $a$ is the thickness of the dielectric claddings and $b$ is the thickness of the air claddings, $\tau$ is a factor which affects the porosity of the Bragg fibre. The value of $\tau$ for point A is smaller than that of point B, and hence the thickness contrast of A is larger than that of B, and in return the porosity corresponding to A is higher than that of B. From equation (8), the bandgap order number $\zeta$ does not affect the thickness contrast, but the absolute values of the cladding thicknesses have a direct relation with $\zeta$. The absolute values of the cladding thicknesses are important parameters in fabrication since every fabrication technique has a limit of processing precision. Using the same parameters as in figure 5, the thicknesses of the dielectric and air cladding can be expressed
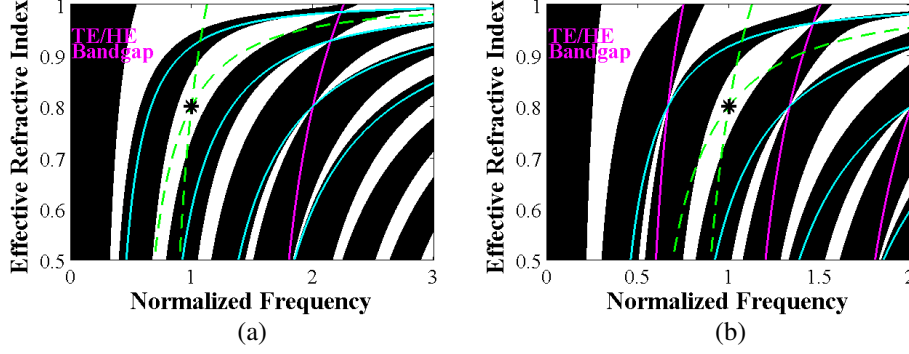
6

Figure 6. SPARROW model curves overlaid upon the TE/HE bandgap. The cyan and magenta solid curves are the dispersion curves of the equivalent isolated cladding layers in the SPARROW model. For both (a) and (b), the intersections of the green dashed curves are the central gap points of the corresponding bandgaps given by the SPARROW, while the black circles are the central gap points predicted by the GHWC. All parameters are the same as that of figure 4 except $n_t = 0.8$. (a) $\tau = 0.25$, $\zeta = 2$. (b) $\tau = 0.5$, $\zeta = 3$.

respectively as $a = \zeta \frac{\tau}{2.382} \lambda_t$ and $b = \zeta \frac{1-\tau}{0.6244} \lambda_t$, indicating that the thicknesses of the claddings are proportional to the bandgap order number $\zeta$. Therefore, the thickness of the claddings can be manipulated by the bandgap order number so as to fit the processing precision of the available fabrication techniques, such as fibre drawing or extrusion.

### 2.3. The central gap points

The central gap points of bandgaps are interesting prominent points, and can be easily manipulated by the GHWC. In figure 4, the maximum point(s) of each order bandgap corresponds to their central gap point(s). In order to verify this argument, we take the stratified planar anti-resonant reflecting optical waveguide (SPARROW) model [51] as a reference method to calculate the central gap points. For instance, the bandgap topologies of points C ($\tau = 0.25, \zeta = 2$) and D ($\tau = 0.5, \zeta = 3$) are shown in figure 6. For better illustration, we choose $n_t = 0.8$. In figure 6, the SPARROW model curves are overlaid upon the TE/HE bandgap diagram. The x-axis is normalized by the frequency of interest $f_t(= c/\lambda_t)$. From figure 6, the central gap point $(f/f_t, n_t)=(1, 0.8)$ predicted by the GHWC is precisely consistent with the value given by the SPARROW model for both cases. This is true for every order of bandgap.

Summarily, one can manipulate the shape of the bandgap in Bragg fibre by using the GHWC, which can efficiently and flexibly manipulate any order of bandgap, while the QWC only predicts the central point of the 1st order bandgap. As discussed, the meaning of each variable in the GHWC is clear. After choosing the materials, for a given effective refractive index of interest $n_t$, any specific central frequency of $\zeta$[th] order bandgap can be archived by tuning $\lambda_t$, and its bandwidth is controlled by the porosity factor $\tau$. This condition works with any combination of materials as long as $n_a > n_b \geq n_c \geq 1$, and it is not only functions well over the terahertz spectrum, but also in other frequency ranges.

### 3. Design of THz Bragg fibre

Both HE$_{11}$ [41, 52, 53] and TE$_{01}$ [44] have been chosen as the operating mode in Bragg fibres. The HE$_{11}$ mode is the fundamental mode in Bragg fibres, which is desirable for single-mode operation, and its linear polarisation makes it easier to couple with other devices. However, in practical designs, support bridges are required to maintain the air gap between the cladding layers. In Bragg fibres using the HE$_{11}$ mode as their operating modes, the support bridges cause significant coupling between the core mode and the surface states, including cladding modes and other modes which are mainly distributed around the bridges. Subsequently, this effect narrows the effective transmission band and increases the propagation loss significantly [41, 52, 53].

We find the negative influence of the support bridges on the performance can be greatly reduced by employing the TE$_{01}$ mode as the operating mode, as detailed in section 3.5. The TE$_{01}$ mode is the first mode with zero azimuthal mode number, and it has a null point in the electric field near the core-cladding interface which prevents the field penetrating into the cladding; this minimizes the negative influence of the support bridges and surface roughness [44], resulting in extremely low propagation loss. In addition, typical single-TE$_{01}$-mode Bragg fibre requires a large core, with many cladding layer periods and a long

Table 2 Material and geometry properties of the target THz Bragg fibre

| Dielectric properties | | | Geometry parameters | | | | Tentative indexes | | | |
|---|---|---|---|---|---|---|---|---|---|---|
| $n_a$* | $n_b$ | $n_c$ | $a$ [µm] | $b$ [mm] | $r_c$ [µm] | N | $\tau$ | $\zeta$ | $n_t$ | $\lambda_t$ [µm] |
| $1.5235+i\kappa_a$ | 1 | 1 | 77.5 | 1.154 | 917.1 | 4 | 0.5 | 1 | 0.997 | 357.29 |

* The frequency dependent complex refractive index of $n_a$ (TOPAS) is obtained from the reference [7]. The extinction coefficient of TOPAS $\kappa_a$ is calculated based on its absorption coefficient $\mu_a$ (dB/cm) $= -0.13 + 0.63(f/1 \times 10^{12}) + (f/1 \times 10^{12})^2$.

transmission distance to filter out the unwanted modes [44]. In this paper, by introducing a new approach using the modal-filtering effect, a low-loss single-$TE_{01}$-mode Bragg fibre can be achieved with a small air core and only 4 cladding layer periods. Besides, the $TE_{01}$ mode has the additional benefit of an immunity to polarisation-mode dispersion from fibre birefringence thanks to it being cylindrically symmetrical and non-degenerate [44]. Moreover, efficient coupling of the $TE_{01}$ mode in a small-core THz Bragg fibre has been reported [54], but the propagation loss of the designed single-$TE_{01}$-mode Bragg fibre in [54] is still as high as 43.4 dB/m.

### 3.1. Bandgap and dispersion curves

Based on the GHWC, the material and geometry properties of the target THz Bragg fibre are listed in table 2. Here, N is the number of photonic crystal periods. In order to locate the minimum propagation loss point of the $TE_{01}$ mode at the centre of the frequency of interest (1 THz), $\lambda_t$ should be tuned carefully around 0.3 mm in practice. By using equation (1) and parameters listed in table 2, the bandgap diagram of the designed THz Bragg fibre is shown in figure 7 (a). Here, we combine the bandgap diagram of TE/HE modes and TM/EH modes in a single diagram. The black (black and grey) regions represent the bandpass region for TE/HE (TM/EH) modes, where the modes are allowed to propagate through the periodic cladding layers and are not confined in the Bragg fibre. On the contrary, the remaining region for each kind of bandgap diagram indicates the bandstop region or so-called bandgap in which the modes are forbidden to pass through the radial photonic crystal structure, and are subsequently confined in the fibre. The horizontal dashed black line is the Brewster line at which the TM/EH bandgaps are always closed completely, and the TE/EH modes have no reflection at the $n_a/n_b$ interface [40]. The solid red box designates the parameter range of the designed THz Bragg fibre and is detailed in figure 7 (b).

In figure 7 (b), the transfer matrix method [55] and finite-element method (using COMSOL) have both been used to independently calculate the dispersion curves. For simplicity, only the dispersion curves of the first six representative modes are plotted, i.e. $HE_{11}$, $TM_{01}$, $HE_{21}$, $TE_{01}$, $EH_{11}$ and $TE_{02}$. $TE_{01}$ is the desired fundamental mode, while $HE_{11}$, $TM_{01}$, $HE_{21}$, $EH_{11}$, and $TE_{02}$ represent the modes competing with $TE_{01}$. Among these competing modes, $HE_{11}$ and $HE_{21}$ are the two lowest-order TE or TE-like (HE) modes, while $TM_{01}$ and $EH_{11}$ are the two lowest order TM or TM-like (EH) modes, and $TE_{02}$ is the second



(a)                                    (b)
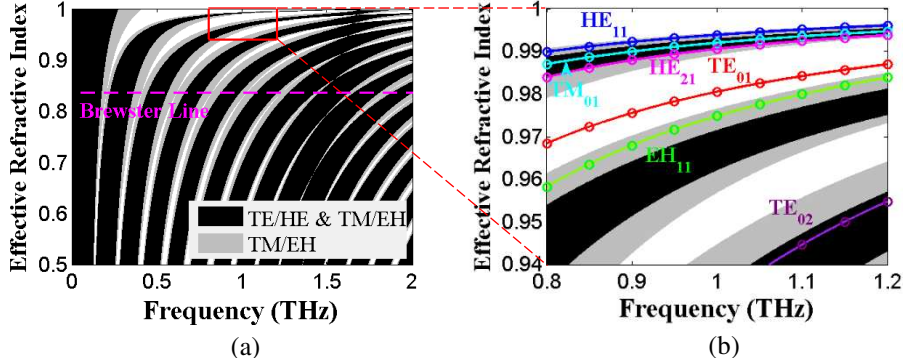
Figure 7. Bandgap and dispersion curves of the target Bragg fibre. (a) Global view of the bandgap. The black (black and grey) region represents the bandpass region for TE/HE (TM/EH) modes. The dashed magenta line is the Brewster line. The red box indicates the region of interest and is detailed in (b). (b) The bandgap and dispersion curves. The blue, cyan, magenta, red, green, and purple solid lines are the theoretical dispersion curves of $HE_{11}$, $TM_{01}$, $HE_{21}$, $TE_{01}$, $EH_{11}$, and $TE_{02}$ modes, respectively, calculated using the transfer matrix method, while the circles with same colours are their corresponding simulation results obtained from COMSOL.

Figure 8. (a) Propagation loss and (b) group velocity dispersion of the Bragg fibre. Solid lines are theoretical results and discrete circles are corresponding simulation results.
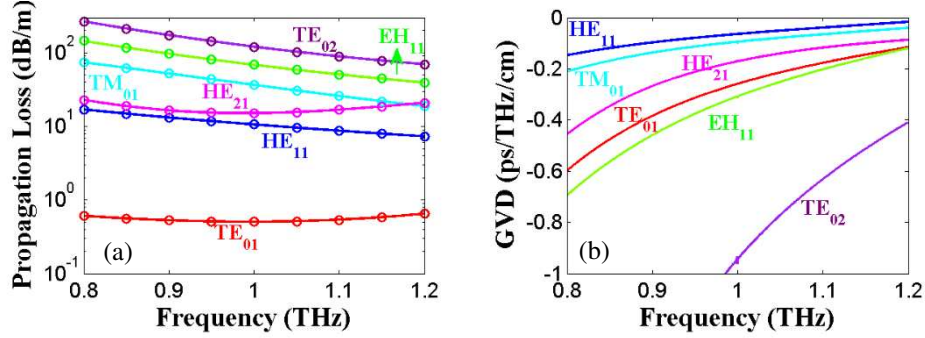


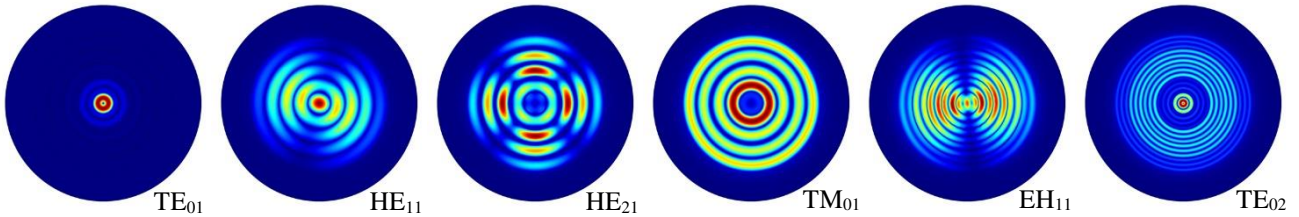TE$_{01}$  HE$_{11}$  HE$_{21}$  TM$_{01}$  EH$_{11}$  TE$_{02}$

Figure 9. Normalized electrical field of the six representative modes at 1 THz. Relevant material and geometry parameters are listed in table 2. The field decreases from red to blue.

mode with zero azimuthal mode number and a similar null point in the electric field near the core-cladding interface. The relative positions of all these modes to the bandgaps affect their propagation loss significantly. These positions are specially designed to enlarge the loss discrimination between the desired TE$_{01}$ mode and its competing modes, which will be detailed in section 3.4.

It is noted that the outermost cladding layer of the Bragg fibre is treated as an absorption layer and there is no signal reflection from the outside. This is achievable in practice by using a thick shielding layer. Hence, in the transfer matrix method, an absorption boundary condition has been used at the interface of the outermost period and the outermost shielding layer as suggested in [55], while in the finite-element method, a perfect-matched layer has been applied.

### 3.2. Propagation loss, GVD, and mode structure

The propagation loss and GVD of the various modes are shown in figure 8. In figure 8 (a), the propagation loss of the desired TE$_{01}$ mode is less than 0.6 dB/m, which is the lowest loss mode across the frequency range of interest (from 0.8 THz to 1.2 THz), while the propagation loss of the main competing mode HE$_{11}$ is more than 11 times greater than that of TE$_{01}$ at the closest frequency points (1.2 THz). It should be noted that the proposed Bragg fibre is a small-core fibre using only 4 cladding layer periods, and that its loss discrimination is even larger than that of a large core fibre with 8 cladding layer periods [44]. The larger loss discrimination is attributed to the modal-filtering effect. Moreover, figure 8 (b) shows that the GVD of the desired TE$_{01}$ mode is less than -0.6 ps/THz/cm. In figures 7 and 8, the numerical simulation results from COMSOL show an excellent consistency with our analytical predictions calculated by the transfer matrix method, supporting the validity and the accuracy of both methods.

The mode patterns at 1 THz are presented in figure 9. It can be seen that the electric field of the desired TE$_{01}$ mode is essentially confined within the lossless air core, while that of the competing modes are leaky, thus experiencing a high signal attenuation introduced by the bulk cladding materials. Subsequently, the TE$_{01}$ mode has significantly less propagation loss from the surface roughness and the support bridges compared to the other competing modes.

### 3.3. Impact of the uncertainty of the refractive index of TOPAS

From 0.2-1.5 THz, the real part of the refractive index of TOPAS in [7] varies in the range of 1.5235±0.0005, while that in [8] varies in the range of 1.5258±0.0002. We note that both measurements were conducted by the same group of researchers across different years. The differences indicate that the real part of the refractive index of TOPAS may thus vary from 1.523 (lower limit in [7]) to 1.526 (upper limit in [8]). Therefore, it is of interest to investigate the impact of this uncertainty of the refractive
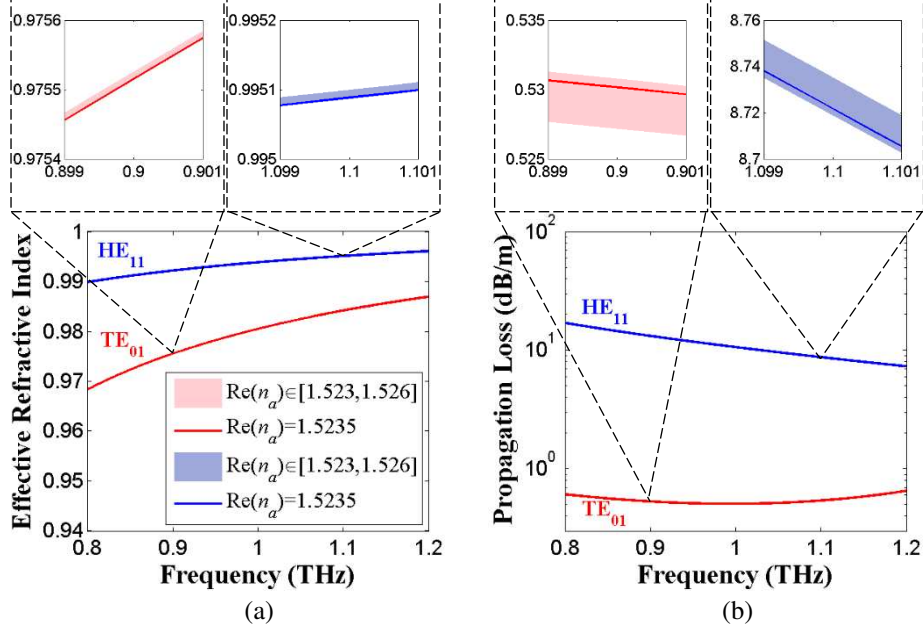
Figure 10. The impact of the uncertainty of the refractive index of TOPAS on the dispersion curves (a) and propagation losses (b) of $TE_{01}$ and $HE_{11}$ modes. The solid red and blue lines corresponds to $Re(n_a) = 1.5235$. The light red and blue regions correspond to $Re(n_a) \in [1.523, 1.526]$. (a) and (b) share the same legend.

index of TOPAS on the dispersion curves and propagation losses in our design. The results from this investigation are shown in figure 10. Here, we use the same geometry parameters as those listed in table 2. As for the absorption coefficient of TOPAS, we use the measurement results in [7] which is slightly greater than that in [8], standing for the case of the highest propagation loss in our design owing to the material absorption within the available parameter range of the absorption coefficient of TOPAS. For simplicity, we consider only the dispersion curves and the propagation losses of the two lowest-loss modes in figure 10. From figures 10 (a) and (b), we can see, respectively, that the impact of the uncertainty of the refractive index of TOPAS ranging from 1.523 to 1.526 on the dispersion curves and propagation losses of the $TE_{01}$ and $HE_{11}$ modes is negligible.

### 3.4. Modal-filtering effect

That the propagation loss of the desired mode should be smaller than that of the other unwanted competing modes is important for the transmission properties of Bragg fibres. Even if several modes are excited at the input, only the desired mode will remain in the Bragg fibre after a certain distance [56] while the other competing modes are heavily attenuated. This strong mode selectivity introduced by the loss discrimination creates a modal-filtering effect and results in an effectively single-mode operation in the Bragg fibre.

There are many factors that contribute to the modal-filtering effect, including the Brewster phenomenon, the confinement loss of each mode, the number of cladding layer periods, and the support bridges. In figure 3, for any combination of cladding layer thicknesses (any value of $\tau$), the TM/EH bandgap always closes up entirely at the Brewster angle, owing to the Brewster phenomenon and ensuring that the bandgap of TM/EH modes is always narrower than that of TE/HE modes, especially near the Brewster line, as exemplified in figure 7. This behaviour of the TM/EH bandgap increases the possibility that the TM/EH modes lie outside the bandgap and become lossy. In addition, the closer the dispersion curve of a guiding mode lies to the edge of the bandgap, the more field penetrates into the claddings, and the higher the confinement loss of it is. Thus, even if the dispersion curves of the TM/EH modes lie inside the bandgap, they are closer to the edge of the bandgap than that of the TE/HE modes, which leads to higher confinement loss. Therefore, the Brewster phenomenon increases the loss of TM/EH modes and increases their loss discrimination with the desired mode.

The confinement loss, in this paper, is defined as the loss due to the scattering of the multilayer claddings only, excluding the material absorption, and hence only the real parts of the refractive indexes of materials have been taken into account in calculating the confinement loss. This should be differentiated from the propagation loss which considers the material
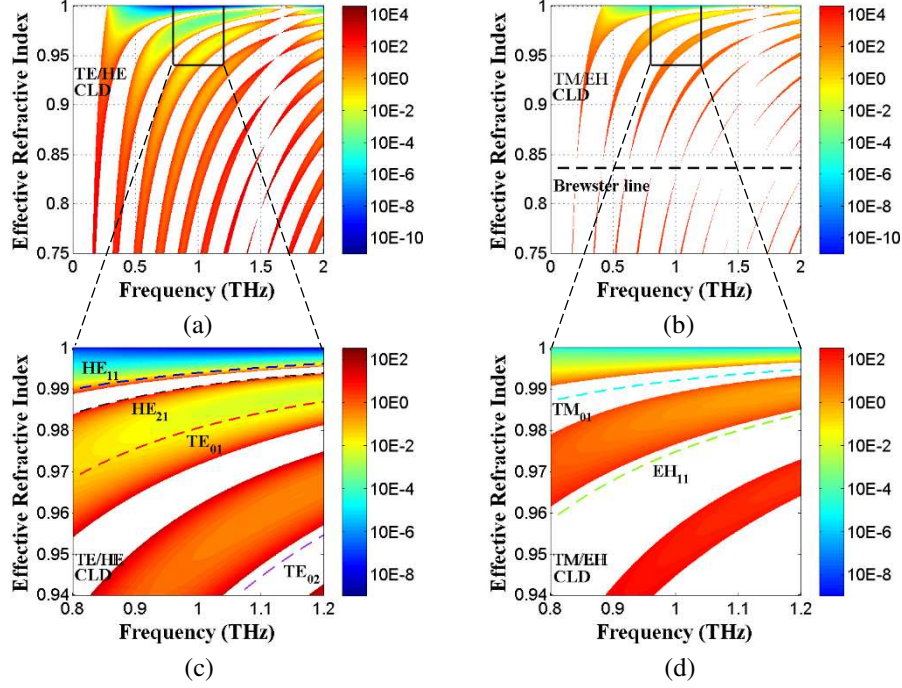
10

Figure 11. Confinement loss diagram in photonic bandgap. The colour map represents the value of confinement losses. The unit is dB/m. The details in the black boxes in (a) and (b) is detailed in (c) and (d), respectively. The dashed blue, black, red, purple, green and cyan lines are the dispersion curves of $HE_{11}$, $HE_{21}$, $TE_{01}$, $TE_{02}$, $TM_{01}$, and $EH_{11}$, respectively.

absorption as well. Owing to the finite number of the cladding layer periods, the guiding modes in the bandstop (or bandgap) region are intrinsically leaky since the confinement is not perfect. This confinement loss, however, decreases exponentially with an increase in the number of the cladding layer periods. We note that this leaky mechanism should not be confused with the leakage of modes in the bandpass region which is determined by Bloch's theorem [47].

To characterize the confinement loss of the designed Bragg fibre, the confinement loss diagram (CLD) [57] and the photonic bandgap are shown together in figure 11. Here, all the parameters of the geometry and the materials are listed in table 2, except that we only use the real part of the complex refractive indexes, since we only consider the scattering loss. The CLD, which presents the confinement loss of the Bragg fibre based on the properties of the geometry and the materials, is independent of any mode. Thus, it is useful to provide a global view of the confinement loss of any Bragg fibre. In addition, as we are only interested inside the bandgap region in regions where the modes can be confined in the Bragg fibre, so the CLD is overlaid with the photonic bandgap diagram. In other words, we only plot the confinement loss inside the bandgap region. The colour map in figure 11 represents the value of the confinement loss in dB/m. Figure 11 (a) is the CLD corresponding to TE and HE modes, while figure 11 (b) corresponds to TM and EH modes. From figures 11 (a) and (b), due to the presence of the Brewster phenomenon for TM and EH modes, the bandgaps of the TM/EH modes are always narrower than that of the TE/HE modes for the same order bandgaps, resulting in higher confinement loss of TM and EH modes compared to that of the TE/HE modes. For all polarisations, the confinement loss in the central region of any order bandgap is always lower than that in the fringe region of the same order bandgap. In addition, for any given frequency, the confinement loss in the central region of the lower order bandgap is less than that of higher order bandgap, while the confinement loss in the fringe region for any order of bandgap is in a similar range. Therefore, it is possible that the confinement loss in the central region of a higher order bandgap is in fact less than that in the fringe region of a lower order bandgap.

The confinement loss diagrams, along with the analytical dispersion curves of TE/HE modes and TM/EH modes are plotted in figures 11 (c) and (d). As was discussed in section 3.1, the relative positions of the six selected modes to the bandgap are significant as they affects the confinement losses of the corresponding modes. It is possible that the confinement loss in the central region of the higher order bandgap is less than that in the fringe region of lower order bandgap. Therefore, based on the GHWC, we have tailored the bandgap to place the $TE_{01}$ mode close to the central region of the 2nd-order bandgap and
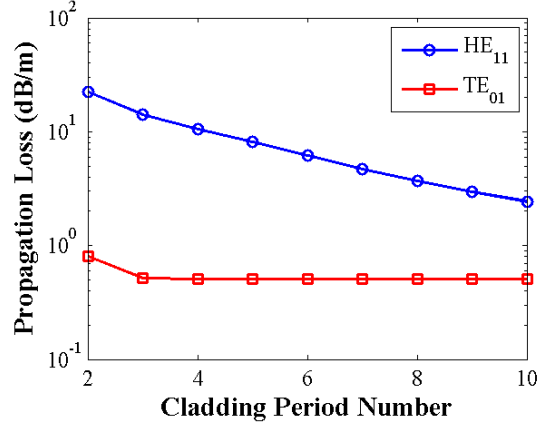
Figure 12. The dependence of the propagation loss at 1 THz of the desired $TE_{01}$ mode and the second lowest loss $HE_{11}$ mode on the number of cladding periods.

meanwhile let the $HE_{11}$ mode be at the edge of $1^{st}$-order bandgap. We also restrict the $TE_{02}$ mode, which has a similar ring field pattern to the $TE_{01}$ mode and can potentially compete mode of $TE_{01}$ mode, to be located outside the bandgap to reduce its impact. In figure 11 (d), both the $TM_{01}$ and $EH_{11}$ mode have been designed to be located outside the bandgap making them very lossy. Within the frequency range of interest, from 0.8 THz to 1.2 THz, compared to the aforementioned six representative modes, other higher order modes are located either in the higher order bandgaps or outside any bandgap resulting in higher confinement loss and weak mode competition. Therefore, the designed Bragg fibre has strong mode selectivity owing to the presence of the photonic bandgap.

According to [58], the propagation loss of the guiding modes in the bandgap region first decreases exponentially with increase in the number of cladding layer periods, following the same exponentially decreasing trend as the confinement loss, and then converges to a constant value due to the limit of the material absorption. Figure 12 illustrates the dependence of the propagation losses at 1 THz of the desired $TE_{01}$ mode and its main competing mode $HE_{11}$ on the number of the cladding layer periods. From figure 12, when the number of the cladding layer periods, N>3, the loss of the $TE_{01}$ mode shows almost no change, while the loss of the $HE_{11}$ mode is still decreasing. As the introduction of support bridges breaks the periodicity of the photonic crystal structure and increases the propagation loss, we limit the number of cladding layer periods to 4 to ensure low loss of the $TE_{01}$ mode. In other words, four periods are sufficient to achieve tight confinement of the desired $TE_{01}$ mode and is a trade-off for the Bragg fibre, because when N>4, the loss discrimination between the desired modes and its competing modes reduces, and the increase of the number of periods does little to reduce the loss of the desired mode.

### 3.5. Impact of the support bridges

The impact of the support bridges on the spectral behaviour of the guided modes is significant. There are many choices in terms of the deployment of the support bridges in a Bragg fibre. Support bridges without symmetry in any two orthogonal directions cause polarisation-mode dispersion. At the same time, it is preferable to have thin and fewer support bridges so as to minimize
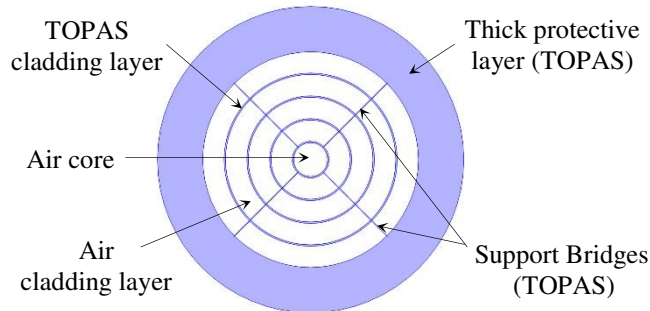


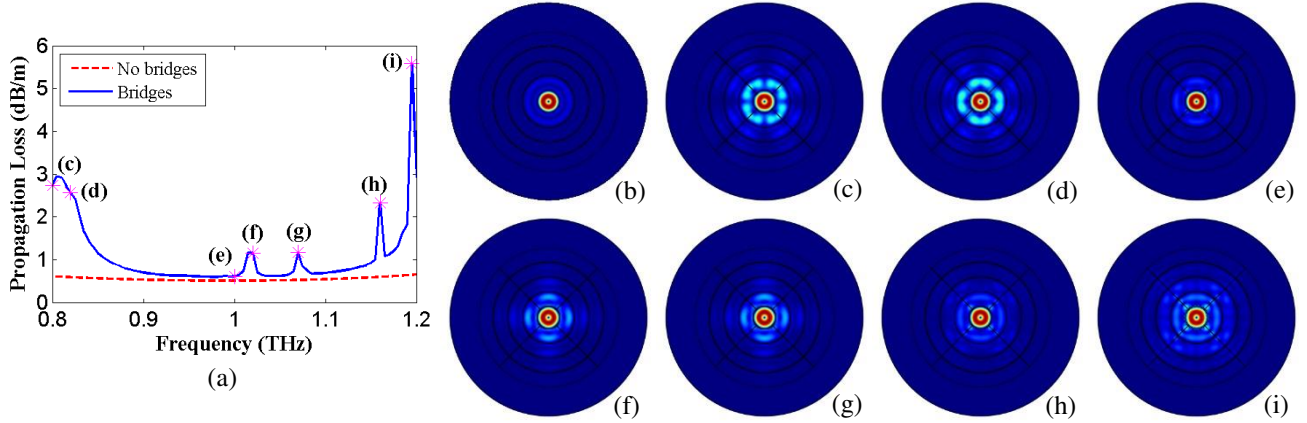Figure 13. Schematic of the practical Bragg fibre with support bridges of width 15 µm.

Figure 14. (a) Propagation loss of $TE_{01}$ mode. (b) is the normalized electrical field of $TE_{01}$ mode at 1THz in ideal Bragg fibre without supportive bridges. (c) – (i) are the normalized electrical field of $TE_{01}$ at 0.8 THz, 0.82 THz, 1 THz, 1.02 THz, 1.07 THz, 1.16 THz, and 1.195 THz, respectively.

their negative impact. However, a trade-off has to be made between the thickness and the layout of the support bridges and the fabrication convenience. Accordingly, the layout of the proposed fibre with support bridges is shown in figure 13. Thanks to the small core, the need for support bridges is significantly reduced compared to designs with a larger core [41]. Here, the width of the support bridges is set to 15 µm, which has been optimized by sweeping the width from 5 µm to 50 µm to reduce the propagation losses of the desired $TE_{01}$ mode over the frequency range from 0.85 THz to 1.15 THz.

Figure 14 (a) shows the propagation loss of the desired $TE_{01}$ mode support bridges. The propagation loss of the $TE_{01}$ mode in the practical Bragg fibre (solid blue line) follows the trend of the ideal Bragg fibre (dotted black line). The deviations between them and some narrow peaks in the practical case are attributed to the presence of the support bridges which break the periodicity of the photonic crystal structure and introduces coupling between the $TE_{01}$ mode and the surface states [43, 53, 59]. The mode structure at several representative frequencies is shown in figures 14 (c) – (i), while figure 14 (b) shows the mode structure of the desired mode without support bridges. It can be clearly seen that compared to the ideal case without bridges, slightly more of the desired field from the $TE_{01}$ mode in the fibre penetrates into the cladding layers, resulting in an increased loss. The coupling between the core mode with the surface states increases the propagation loss significantly, which also decreases the effective bandwidth of the Bragg fibre and so is undesirable. Nonetheless, the propagation loss of the designed Bragg fibre with support bridges is still less than 1.2 dB/m from 0.85 THz to 1.15 THz with a minimum of 0.5953 dB/m at 0.98 THz.

Thanks to the special mode structure of the $TE_{01}$ mode with a null point in electric field near the interface between the core and the cladding, the support bridges in our design only slightly increase the propagation loss of the desired $TE_{01}$ mode, while causing weak coupling between the core mode and the surface states. In addition, compared to the larger core scheme in [44], the utilization of a second order bandgap to confine the desired $TE_{01}$ mode in our design greatly reduces the diameter of the core. Subsequently, it reduces the size of the fibre, reducing the need for and negative impact from support bridges, and hence should be beneficial to fabrication.

## 4. CONCLUSION

This paper presents a detailed analytical and numerical study of a tightly confined single-$TE_{01}$-mode small-air-core terahertz Bragg fibre which exhibits both low loss and low dispersion. Firstly, we have proposed a generalized half-wavelength condition (GHWC) which relates the photonic bandgap with the material and geometry properties, promoting the manipulation of the photonic bandgap in the Bragg fibre effectively. The properties of different order photonic bandgaps in the Bragg fibre have been investigated.

Secondly, the modal-filtering effect which contributes to increased discrimination by loss between the desired fundamental modes and other high order unwanted competing modes has been investigated, which allows the fibre to operate in an effectively single-mode fashion. The factors contributing to the modal-filtering effect have also been discussed.

Thirdly, we propose the use of the modal-filtering effect in a novel way. We tailor the bandgap by using the generalized half-wavelength condition to let the desired $TE_{01}$ mode be located near the central region of the second order bandgap, while maintaining loss discrimination between the desired $TE_{01}$ mode and other unwanted competing modes. This reduces the required diameter of the core and hence reduces the size of the fibre. It also reduces the need for support bridges, aiding fabrication.

Finally, based on our analysis, we propose the design of a tightly confined single-$TE_{01}$-mode small-air-core Bragg fibre with propagation loss and GVD less than 1.2 dB/m and -0.6 ps/THz/cm respectively over a frequency range from 0.85 THz to 1.15 THz, presenting significant potential improvements compared to existing single-mode THz Bragg fibres. Having now determined an optimised structure for a THz Bragg fibre, our work is focusing on a number of fabrication methods.

**Acknowledgements**

**References**

[1] V.R. Almeida, Q. Xu, C.A. Barrios, and M. Lipson, "Guiding and confining light in void nanostructure," *Opt. Lett.*, vol. 29, no. 11, pp. 1209-1211, Jun. 2004.

[2] T. Monro, "Optical fibres: Beyond the diffraction limit," *Nat. Photon.*, vol. 1, no. 2, pp. 89-90, Feb. 2007.

[3] A. Argyros, "Microstructures in polymer fibres for optical fibres, THz waveguides, and fibre-based metamaterials," *ISRN Optics*, Feb. 2013.

[4] S. Atakaramians, S. Afshar, T. M. Monro, and D. Abbott,"Terahertz dielectric waveguides," *Adv. Opt. Photonics*, vol. 5, no. 2, pp. 169-215, Jun. 2013.

[5] S. R. Andrews, "Microstructured terahertz waveguides," *J. Phys. D Appl. Phys.*, vol. 47, no. 37, p. 374004, Aug. 2014.

[6] A. Argyros, "Microstructured polymer optical fibers," *J. Lightw. Technol.,* vol. 27, no. 11, pp. 1571-1579, Jun. 2009.

[7] H. Bao, K. Nielsen, H. K. Rasmussen, P.U. Jepsen, and O. Bang, "Fabrication and characterization of porous-core honeycomb bandgap THz fibers," *Opt. Exp.*, vol. 20, no. 28, pp. 29507-29517, Dec. 2012.

[8] K. Nielsen, H. K. Rasmussen, A. J. Adam, P. C. Planken, O. Bang, and P. U. Jepsen, "Bendable, low-loss Topas fibers for the terahertz frequency range," *Opt. Exp.*, vol. 17, no. 10, pp. 8592-8601, May 2009.

[9] J. Anthony, R. Leonhardt, A. Argyros, and M. C. Large, "Characterization of a microstructured Zeonex terahertz fiber". *JOSA B*, vol. 28, no. 5, pp. 1013-1018, May 2011.

[10] S. Atakaramians, S. Afshar, H. Ebendorff-Heidepriem, M. Nagel, B. M. Fischer, D. Abbott, and T. M. Monro, "THz porous fibers: design, fabrication and experimental characterization," *Opt. Exp*, vol. 17, no. 16, pp. 14053-14062, Aug. 2009.

[11] J. Y. Lu, C. P. Yu, H. C. Chang, H. W. Chen, Y. T. Li, C. L. Pan, and C. K. Sun, "Terahertz air-core microstructure fiber," *Appl. Phys. Lett.*, vol. 92, no. 6, p. 064105. Feb 2008.

[12] B. Hong, N. Somjit, J. Cunningham, and I. Robertson, "Design study of low loss single-mode hollow core photonic crystal terahertz waveguide with support bridges," In *40th Int. Conf. Infrared, Millim. THz Waves , 2015 (IRMMW-THz 2015)*, pp. 1-2, Aug. 2015.

[13] S. Atakaramians, S. Afshar V, M. Nagel, H. K. Rasmussen, O. Bang, T. M. Monro, and D. Abbott, "Direct probing of evanescent field for characterization of porous terahertz fibers," *Appl. Phys. Lett.*, vol. 98, no. 12, p. 121104 Mar. 2011.

[14] J. Anthony, R. Leonhardt, S. G. Leon-Saval, and A. Argyros, "THz propagation in kagome hollow-core microstructured fibers," *Opt. Exp.*, vol. 19, no. 19, pp. 18470-18478, Sep. 2011.

[15] A. Dupuis, A. Mazhorova, F. Désévédavy, M. Rozé, and M. Skorobogatiy, "Spectral characterization of porous dielectric subwavelength THz fibers fabricated using a microstructured molding technique," *Opt. Exp.*, vol. 18, no. 13, pp. 13813-13828, Jun. 2010.

[16] Z. Wu, W. R. Ng, M. E. Gehm, and H. Xin, "Terahertz electromagnetic crystal waveguide fabricated by polymer jetting rapid prototyping," *Opt. Exp.*, vol. 19, no. 5, pp. 3962-3972, Feb. 2011.

[17] A. Dupuis, K. Stoeffler, B. Ung, C. Dubois, and M. Skorobogatiy, "Transmission measurements of hollow-core THz Bragg fibers," *JOSA B*, vol. 28, no. 4, pp. 896-907, Apr. 2011.

[18] M.Skorobogatiy, and A. Dupuis, "Ferroelectric all-polymer hollow Bragg fibers for terahertz guidance," *Appl. Phys. Lett.*, vol. 90, no. 11, p. 113514, Mar. 2007.

[19] C. S. Ponseca Jr, R. Pobre, E. Estacio, N. Sarukura, A. Argyros, M. C. Large, and M. A. van Eijkelenborg, "Transmission of terahertz radiation using a microstructured polymer optical fiber," *Opt. Lett.*, vol. 33, no. 9, pp. 902-904, May 2008.

[20] H. Han, H. Park, M. Cho, and J. Kim, "Terahertz pulse propagation in a plastic photonic crystal fiber," *Appl. Phys. Lett.*, vol. 80, no. 15, pp. 2634-2636, Apr 2002.

[21] V. Setti, L. Vincetti, and A. Argyros, "Flexible tube lattice fibers for terahertz applications," *Opt. Exp.*, vol. 21, no. 3, pp. 3388-3399, Feb, 2013.

[22] C. D. Nordquist, M. C. Wanke, A. M. Rowen, C. L. Arrington, M. Lee, and A. D. Grine, "Design, fabrication, and characterization of metal micromachined rectangular waveguides at 3 THz," In *2008 IEEE AP-S Int. Symp.*, pp. 1-4, Jul. 2008.

[23] T. Ito, Y. Matsuura, M. Miyagi, H. Minamide, and H. Ito, "Flexible terahertz fiber optics with low bend-induced losses," *JOSA B*, vol. 24, no. 5, pp. 1230-1235. May 2007.

[24] H. Bao, K. Nielsen, O. Bang, and P. U. Jepsen, "Dielectric tube waveguides with absorptive cladding for broadband, low-dispersion and low loss THz guiding," *Sci. Rep.*, vol. 5, p. 7620, Jan 2015.

[25] T. I.Jeon, and D. Grischkowsky, "Direct optoelectronic generation and detection of sub-ps-electrical pulses on sub-mm-coaxial transmission lines," *Appl. Phys. Lett.*, vol. 85, no. 25, pp. 6092-6094, Dec 2004.

[26] J. Y. Yin, J. Ren, H. C. Zhang, B. C. Pan，and T. J. Cui, "Broadband frequency-selective spoof surface plasmon polaritons on ultrathin metallic structure," *Sci. Rep.*, vol. 5, p. 8165, Feb, 2015.

[27] Y. Q. Liu, L. B. Kong, C. H. Du,and P. K. Liu, "Spoof surface plasmon modes on doubly corrugated metal surfaces at terahertz frequencies," *J. Phys. D Appl. Phys.*, vol. 49, no. 23, p. 235501, May 2016.

[28] K. Wang, and D. M. Mittleman, "Metal wires for terahertz wave guiding," *Nature*, vol. 432, no. 7015, pp. 376-379, Nov 2004.

[29] H. Pahlevaninezhad, T. E. Darcie, and B. Heshmat, "Two-wire waveguide for terahertz," *Opt. Exp.*, vol. 18, no. 7, pp.7415-7420, Mar. 2010.

[30] A. Dupuis, J. F. Allard, D. Morris, K. Stoeffler, C. Dubois, and M. Skorobogatiy, "Fabrication and THz loss measurements of porous subwavelength fibers using a directional coupler method," *Opt. Exp.*, vol. 17, no. 10, pp. 8012-8028, May 2009.

[31] R. Mendis, and D. Grischkowsky, "Undistorted guided-wave propagation of subpicosecond terahertz pulses," *Opt. Lett.*, vol. 26, no. 11, pp. 846-848, Jun. 2001.

[32] M. Mbonye, R. Mendis, and D. M. Mittleman, "Measuring TE1 mode losses in terahertz parallel-plate waveguides," *J. Infrared Millim. Terahertz Waves*, vol. 34, pp. 416-422, Aug. 2013.

[33] M. Navarro-Cía, M. S. Vitiello, C. M. Bledt, J. E. Melzer, J. A. Harrington, and O. Mitrofanov, "Terahertz wave transmission in flexible polystyrene-lined hollow metallic waveguides for the 2.5-5 THz band," *Opt. Exp.*, vol. 21, no. 20, pp. 23748-23755, Oct 2013.

[34] O. Mitrofanov, R. James, F. A. Fernández, T. K. Mavrogordatos, and J. A. Harrington, "Reducing transmission losses in hollow THz waveguides," *IEEE Trans. THz Sci. Technol.,* vol. 1, no. 1, pp. 124-132. Sep. 2011.

[35] M. Bozzi, A. Georgiadis, and K. Wu, "Review of substrate-integrated waveguide circuits and antennas," *IET Microw. Antenna P.,* vol. 5, no. 8, pp. 909-920, Jun 2011.

[36] L. Jin, R. M. A. Lee, and I. Robertson, "Analysis and design of a novel low-loss hollow substrate integrated waveguide, " *IEEE Trans. Microw. Theory Tech.,* vol. 62, no. 8, pp. 1616–1624, Aug. 2014

[37] A. L. Bingham, and D. R. Grischkowsky, "Terahertz 2-D photonic crystal waveguides," *IEEE Microw. Compon. Lett.,* vol. 18, no. 7, pp. 428-430, Jul. 2008.

[38] K. Tsuruda, M. Fujita, and T. Nagatsuma, "Extremely low-loss terahertz waveguide based on silicon photonic-crystal slab," *Opt. Exp.*, vol. 23, no. 25, pp. 31977-31990, Dec 2015.

[39] T. Nagatsuma, S. Hisatake, M. Fujita, H. H. N. Pham, K. Tsuruda, S. Kuwano, and J. Terada, " Millimeter-wave and terahertz-wave applications enabled by photonics," *IEEE J. Quantum Electron*, vol. 52, no. 1, pp. 1-12, Jan 2016.

[40] P. Yeh, A. Yariv, and E. Marom, "Theory of Bragg fiber," *JOSA*, vol. 68, no. 9, pp. 1196-1201, Sep. 1978.

[41] G. Vienne, Y. Xu, C. Jakobsen, H. J. Deyerl, J. B. Jensen, T. Sørensen, T. P. Hansen, Y. Huang, M. Terrel, R. K. Lee, and N. A. Mortensen, "Ultra-large bandwidth hollow-core guiding in all-silica Bragg fibers with nano-supports," *Opt. Exp.*, vol. 12, no. 15, pp. 3500-3508, July 2004.

[42] B. Temelkuran, S. D. Hart, G. Benoit, J. D. Joannopoulos, and Y. Fink, "Wavelength-scalable hollow optical fibres with large photonic bandgaps for CO2 laser transmission," *Nature*, vol. 420, no. 6916, pp. 650-653. Dec 2002.

[43] J. A. West, C. M. Smith, N. F. Borrelli, D. C. Allan, and K. W. Koch, "Surface modes in air-core photonic band-gap fibers," *Opt. Exp.*, vol. 12, no. 8, pp. 1485-1496, Apr. 2004.

[44] S. G. Johnson, M. Ibanescu, M. Skorobogatiy, O. Weisberg, T. D. Engeness, M. Soljačić, S. A. Jacobs, J. D. Joannopoulos, and Y. Fink, "Low-loss asymptotically single-mode propagation in large-core OmniGuide fibers," *Opt. Exp.*, vol. 9, no. 13. pp. 748-779, Dec. 2001.

[45] Y. Fink, J. N. Winn, S. Fan, C. Chen, J. Michel, J. D. Joannopoulos, and E. L. Thomas, "A dielectric omnidirectional reflector," *Science*, vol. 282, no. 5394, pp. 1679-1682, Nov. 1998.

[46] Y. Zhang, and I. D. Robertson, "Single-mode terahertz Bragg fiber design using a modal filtering approach," *IEEE Trans. Microw. Theory Tech.,* vol. 58, no. 7, pp. 1985-1992, Jul. 2010.

[47] A. Kitagawa, and J. I. Sakai, "Bloch theorem in cylindrical coordinates and its application to a Bragg fiber," *Phys. Rev. A.,* vol. 80, no. 3, p. 033802, Sep. 2009.

[48] Y. Xu, G. X. Ouyang, R. K. Lee, and A. Yariv, "Asymptotic matrix theory of Bragg fibers," *J. Lightw. Technol.,* vol. 20, no. 3, p. 428, Mar. 2002.

[49] J. I. Sakai, "Analytical expression of confinement loss in Bragg fibers and its relationship with generalized quarter-wave stack condition," *JOSA B*, vol. 28, no. 11, pp. 2740-2754, Nov. 2011.

[50] J. Dai, J. Zhang, W. Zhang, and D. Grischkowsky, "Terahertz time-domain spectroscopy characterization of the far-infrared absorption and index of refraction of high-resistivity, float-zone silicon," *JOSA B*, vol. 21, no. 7, pp. 1379-1386, Jul. 2004.

[51] K. J. Rowland, S. Afshar, and T. M. Monro, "Bandgaps and antiresonances in integrated-ARROWs and Bragg fibers; a simple model," *Opt. Exp.*, vol. 16, no. 22, pp. 17935-17951, Oct. 2008.

[52] C. M. Smith, N. Venkataraman, M. T. Gallagher, D. Müller, J. A. West, N. F. Borrelli, D. C. Allan, and K. W. Koch, "Low-loss hollow-core silica/air photonic bandgap fibre," *Nature*, vol. 424, no. 6949, pp. 657-659, Aug. 2003.

[53] A. Hassani, A. Dupuis, and M. Skorobogatiy, "Porous polymer fibers for low-loss Terahertz guiding," *Opt. Exp.*, vol. 16, no. 9, pp. 6340-6351, Apr. 2008.

[54] H. Y. Yao, J. Y. Jiang, Y. S. Cheng, Z. Y. Chen, T. H. Her, and T. H. Chang, "Modal analysis and efficient coupling of TE 01 mode in small-core THz Bragg fibers," *Opt. Exp.*, vol. 23, no. 21, pp. 27266-27281, Oct 2015.

[55] S. Guo, S. Albin, and R. Rogowski, "Comparative analysis of Bragg fibers," *Opt. Exp.*, vol. 12, no. 1, pp. 198-207. Jan. 2004.

[56] M. Ibanescu, S. G. Johnson, M. Soljačić, J. D. Joannopoulos, Y. Fink, O. Weisberg, T. D. Engeness, S. A. Jacobs, and M. Skorobogatiy, "Analysis of mode structure in hollow dielectric waveguide fibers," *Phys. Rev. E*, vol. 67, no. 4, p.046608, Apr. 2003.

[57] Y. Zhang, and I. D. Robertson, "Analysis and design of Bragg fibers using a novel confinement loss diagram approach," *J. Lightw. Technol.,* vol. 28, no. 22, pp.3197-3206, Nov. 2010.

[58] J. I. Sakai, and N. Nishida, "Confinement loss, including cladding material loss effects, in Bragg fibers," *JOSA B*, vol. 28. no. 3, pp. 379-386, Mar. 2011.

[59] F. Poli, M. Foroni, D. Giovanelli, A. Cucinotta, S. Selleri, J. B. Jensen, J. Lægsgaard, A. Bjarklev, G. Vienne, C. Jakobsen, and J. Broeng, "Silica bridge impact on hollow-core Bragg fiber transmission properties," In *Opt. Fiber Commun. Conf.,* Anaheim, CA, p. OML8, Mar. 2007.